An improved pixel-based water vapor tomography model

Yibin Yao [1, 2, *], Linyang Xin [1] and Qingzhi Zhao [3]

[1]   School of Geodesy and Geomatics, Wuhan University, Wuhan 430079, China;
     ybyao@whu.edu.cn (Y.Y); linyangxin@whu.edu.cn (L.X);
[2]   Key Laboratory of Geospace Environment and Geodesy, Ministry of Education, Wuhan University, Wuhan 430079, China
[3]   College of Geomatics, Xi'an University of Science and Technology, Xi'an 710054, China;
     zhaoqingzhia@163.com
*   Correspondence: ybyao@whu.edu.cn; Tel.: +86-027-68758401

Abstract: As a new detection method of three-dimensional water vapor, the ground-based water vapor tomography technique using Global Navigation Satellite Systems (GNSS) observations can obtain the high spatial and temporal distribution information of tropospheric water vapor. Since the troposphere tomography was proposed, most previous studies belong to the pixel-based method, dividing the interest area into three-dimensional voxels of which the water vapor density of each voxel center is taken as the average water vapor density. However, the abovementioned method can only find the water vapor density value of the center of each voxel, which is unable to express the continuous change of water vapor in space and destroys the spatial continuity of the water vapor variation. Moreover, when using the pixel-based method, too many voxels are needed to express the water vapor density, which leads to the problem of too many coefficients to be estimated. After analyzing the limitations of the traditional pixel-based tropospheric tomography technique, this paper proposes an improved pixel-based GNSS tropospheric water vapor tomography model. The tomographic experiments were validated using the data from 11 GNSS stations from the Hong Kong Satellite Positioning Reference Station Network (SatRef) collected between 25 March and 25 April 2014. The comparison between tomographic results and the European Centre for Medium-Range Weather Forecasts (ECMWF) data is mainly used to analyze the accuracy of the new improved model under different conditions, for showing that this improved model is superior to the traditional pixel-based model in terms of root-mean-square error (RMSE) and bias. The tomography water vapor profiles of the improved model were also evaluated using radiosonde data to show the efficiency of the proposed model. Results show that the new model has more advantages than the traditional pixel-based model on the RMSE, especially when obtaining the water vapor in voxels without the penetration of GNSS rays, which is improved by 5.88%. This improved model also solves the aforesaid limitations with more ease and convenience in expression.

Keywords: GNSS; water vapor tomography; ECMWF; Radiosonde

1. Introduction

The distribution of water vapor is complex and highly variable, and water vapor, as the most active key component of the atmosphere, is indeed hard to describe accurately (Rocken et al., 1997). An in-depth understanding of temporal and spatial variation of water vapor plays an important role in improving the accuracy of weather forecasting and early warning of disastrous weather (Weckwerth et al., 2004).

GNSS water vapor monitoring techniques can not only acquire the two-dimensional spatial and temporal distribution of water vapor in the horizontal direction (Bevis et al., 1994; Emardson et al., 1998; Baltink et al., 2002; Bock et al., 2005) but can also use a three-dimensional tomography method to reconstruct the vertical structure of water vapor at high temporal-spatial resolution (Flores et al., 2000; Seko et al., 2000; Macdonald et al., 2002).

Braun et al. (1999) first proposed the concept of reconstructing the tropospheric water vapor structure using 20 GPS stations in a regional observational network. Flores et al. (2000) first presented a method of recovering the slant wet delay (SWD) and obtained the water vapor density using the observation of SWD by singular value decomposition (SVD) combined with a least square method. In the same year, Hirahara (2000) used different methods to conduct tropospheric tomography experiments, which also confirmed the feasibility of obtaining three-dimensional water vapor fields using GPS technology. Since then, many scholars have studied GNSS troposphere tomography techniques and completed many research experiments (Rohm et al., 2014; Yao et al., 2016; Ding et al., 2018; Zhao et al., 2018).

Regarding the tropospheric tomography model solution and algorithm improvement, Hirahara (2000) conducted a four-dimensional tropospheric wet refractivity retrieval of the GPS network from Shigaraki and solved the observation equations using the damping least square method, which is commonly used in seismic tomography. Braun et al. (2003, 2004) overcame the sensitivity problem in tomographic results by using the extended sequential filtering method. Perler et al. (2011) presented a new parameterization method for the water vapor retrieval. The measured and simulated data proved that this method can obtain better tomographic solution results of water vapor. Nilsson and Gradinarsky (2006) obtained the tropospheric tomographic results directly from the original GNSS phase observations combined with the Kalman filter method. Rohm and Bosy (2009) used the Moore-Penrose pseudo-inverse of variance-covariance to solve the linear equations and emphasized the ill-posed tomography equation. Zhao and Yao (2017) obtained good results by using the optimal grid-making method for water vapor tomography. In the meantime, a method of using the side-penetrating signals for tomography was proposed to improve the effect of GNSS ray utilization rate. Aghajany and Amerian (2017) obtained the tomography results of water vapor profiles, applying 3D ray tracing technique based on Eikonal equations and ERA-I numerical weather prediction data to perform the signal path. Dong and Jin (2018) reconstructed the 3-D water vapor density using the combined multi-GNSS system, showing that the accuracy of GNSS tropospheric tomography results could be improved by 5% from the GPS-only system to the dual-system (GPS+GLONASS). Besides, the virtual reference station approach (Vollath et al., 2013; Marel, 1998), an effective method to attenuate the effects of atmospheric errors in long-distance dynamic positioning, could also be used in GNSS tropospheric tomography.

Although GNSS tomography techniques have been developed for more than two decades, it has been challenging to enhance the water vapor quality and the stability of the solution results through the multi-system and multi-source data combination method and improve the solution and algorithm of the tropospheric tomography model. However, in the previous studies, most water vapor tomography methods belong to the pixel-based model, which means that the three-dimensional meshes of the study area were

80 used, and the water vapor density at the center of each voxel was taken as the average water vapor density
81 of the whole voxel. Only could find the water vapor density value of the center of each voxel, the pixel-
82 based tomography is unable to continuously express the change of water vapor in space and also breaks the
83 spatial continuity of water vapor. Since the three-dimensional water vapor density is stored through the
84 voxels, a large amount of voxel information (the spatial position, the water vapor density within the voxel,
85 etc.) is required when describing the spatial water vapor density distribution, which is inconvenient for later
86 use (Yao et al., 2013). What's more, though some constraints could be put on apriori models in order to
87 overcome the ill-posed problem in the pixel-based tomography, some errors due to empirical constraints
88 would be added artificially. Thus, this paper analyzes the limitations of the traditional pixel-based
89 tropospheric tomography and proposes an improved pixel-based water vapor tomography model. This
90 model combines the advantages of facilitating the continuity of water vapor expression in spatial-temporal
91 distribution efficiently and retrieving the three-dimensional water vapor distribution in the interest region
92 easily. The experimental results show that the accuracy of the improved model is enhanced, and the new
93 model has more advantages when obtaining water vapor in voxels without GNSS rays penetrating. Under
94 strong rainfall weather conditions, the tomographic results of the improved model are more stable and
95 reliable.

96 **2. An improved pixel-based tropospheric tomography model**
97 *2.1. Establishment of the traditional tropospheric tomography model*
98 2.1.1. Retrieval of SWV
99   For tropospheric tomography, the most important observation is the slant water vapor (SWV), which
100 is related to the water vapor density and can be defined by

101 $$SWV = \int_S \rho_V \, ds \quad (1)$$

102 where *s* represents the path of the satellite signal ray, and ρ_V is the water vapor density (units: g/m^3).

103 SWV can be obtained by the following method:

104 $$SWV = \frac{10^6}{R_\omega [(k_3 / T_m) + k_2']} \cdot SWD \quad (2)$$

105 where k_2' =16.48 K hPa^{-1}, k_3=3.776×10^5 K^2 hPa^{-1}, and R_ω =461 J kg^{-1} K^{-1}, which represent the specific

106 gas constants for water vapor. T_m is the weighted mean tropospheric temperature, calculated from an

107 empirical equation proposed by Liu et al. (2001) using the meteorological measurements. SWD is the slant
108 wet delay, which may be given as

109 $$SWD_{elv,\varphi} = m_{wet}(elv) \times ZWD + m_{wet}(elv) \times \cot(elv) \times (G_{NS}^w \times \cos\varphi + G_{EW}^w \times \sin\varphi) + R \quad (3)$$

110 where *elv* is the satellite elevation, *φ* is the azimuth, m_{wet} is the wet mapping function, G_{NS}^w and G_{EW}^w

111 are the wet delay gradient parameters in the north-south and east-west directions, respectively. *R* refers to
112 the unmodeled zero difference residuals that may involve unmodeled influence on the three-dimensional
113 spatial water vapor distribution, which can make up for the lack of tropospheric anisotropy using only the
114 gradient term (Bi et al., 2006). Since the GAMIT software only provides the double difference residuals,

115 the zero difference residuals in this paper are obtained from the double difference residuals according to

116 the method proposed by Alber et al. (2000). ZWD is the zenith wet delay, which is extracted from the zenith

117 tropospheric delay (ZTD) by separating the zenith hydrostatic delay (ZHD) using equation ZWD=ZTD-

118 ZHD. ZHD can be calculated precisely using surface pressure based on the Saastamoinen model

119 (Saastamoinen, 1972):

120
$$ZHD = \frac{0.002277 \times P_s}{1 - 0.00266 \times \cos(2\varphi) - 0.00028 \times H} \quad (4)$$

121 where P_s is the surface pressure (unit: hPa), φ is the latitude of the station, and H is the geodetic

122 height (unit: km). The unit of ZHD is meter.

123 Since the SWV is obtained, the tomographic area can be discretized into a number of voxels, in which

124 the water vapor density is a constant during a given period of time. Therefore, a linear equation relating the

125 SWV and the water vapor density can be established as follows (Chen and Liu, 2014):

126

127
$$SWV^p = \sum_{ijk}(D_{ijk}^p \cdot \rho_{ijk}) \quad (5)$$

128 where SWV^p is the slant water vapor of ρ th signal path (unit: mm). i, j, and k are the positions of

129 discrete tomographic voxels in the longitudinal, latitudinal and vertical directions, respectively. D_{ijk}^p is

130 the distance of the ρ th signal in voxel (i, j, k) (unit: km). ρ_{ijk} is the water vapor density in a given voxel

131 (i, j, k) (unit: g/m^3). A matrix form of this observation equation can be rewritten as follows (Flores et al.,

132 2000; Chen and Liu, 2014):

133
$$y_{m \times 1} = A_{m \times n} \cdot \rho_{n \times 1} \quad (6)$$

134 where *m* is the number of total SWVs, and *n* is the number of voxels in the tomographic area. *y* is the

135 observed value here as the SWV, which penetrates the whole interest area, *A* is the coefficient matrix of the

136 signal transit distances through the voxels, and ρ is the column vector of the unknown water vapor

137 density.

138 2.1.2. Constraint equations of the tomography modeling

139 Solving for the unknown water vapor density in Eq. (6) is actually an inversion algorithm issue as the

140 design matrix A is a large sparse matrix, whose normal equation is singular, leading to numerical problems

141 when using a direct inversion method (Bender et al., 2011). To overcome this rank deficiency problem,

142 constraint equations are often introduced to the tomography equation (Flores et al., 2000; Troller et al.,

143 2002; Rohm and Bosy, 2009; Bender et al., 2011). In our study, the horizontal constraint equation is imposed

144 by the Gauss-weighted functional method (Guo et al., 2016) and the vertical constraint equation is imposed

145 by the functional relationship of the exponential distribution (Cao, 2012), respectively. The final

146 tomography model is then obtained as

4

147
$$\begin{pmatrix} A_{m \times n} \\ H_{m \times n} \\ V_{m \times n} \end{pmatrix} \bullet \rho_{n \times 1} = \begin{pmatrix} y_{m \times n} \\ 0_{m \times n} \\ 0_{m \times n} \end{pmatrix} \qquad (7)$$

148 where H and V are the coefficient matrices of horizontal and vertical constrains, respectively. In order to
149 obtain the inverse matrix shown in Eq. (7), singular value decomposition is used in this paper (Flores et al.,
150 2000).

151 *2.2. An improved pixel-based water vapor tomography model*

152   The improved tomography model proposed in this paper can take full advantage of facilitating the
153 continuity of water vapor expression efficiently in spatial-temporal distribution and calculating the water
154 vapor density conveniently. The improved tomography model begins to obtain the water vapor density
155 saved as the observation value from voxels penetrated by GNSS rays using the traditional pixel-based
156 tomography model and then obtains the optimal polynomial function of each layer through adaptive training.
157 Using the optimal polynomial fitting function of each layer with known coefficients, the water vapor density
158 can finally be calculated in any tomographic region by given the latitude, longitude and the altitude. Specific
159 steps are as follows:

160   First, use the traditional pixel-based water vapor tomography model to obtain the initial water vapor
161 density from voxels penetrated by GNSS rays as the observation values for obtaining the optimal
162 polynomial function coefficients of each layer.

163   Second, normalize the coordinates of each voxel center in the tomographic area. Since the polynomial
164 fitting of the water vapor at each tomographic layer is in essence establishing the relationship between the
165 latitude as well as the longitude of the tomographic region and the water vapor density. The general
166 expression is:

167
$$V_d = a_0 + a_1 B + a_2 L + a_3 BL + a_4 B^2 + a_5 L^2 + a_6 B^2 L \cdots \quad (8)$$

168 where B is the latitude, L is the longitude, and V_d represents the water vapor density. Polynomial

169 coefficients such as a_i are obtained via the least squares method. In the process of solving, because the
170 numerical values of the latitude and longitude are not small, the magnitude of multiple power may be larger
171 than 10^4, which will lead to the ill-posed problem of the design matrix in the inversion process and affect
172 the reliability of the estimated coefficients. To ensure that the design matrix constructed will be relatively
173 stable in the inversion process, the latitude and longitude coordinates B and L need to be normalized. The
174 specific methods are as follows:

175
$$B^* = \frac{B - \mu_B}{\sigma_B}$$
$$L^* = \frac{L - \mu_L}{\sigma_L} \qquad (9)$$

176 where B^* and L^* are the normalized latitude and longitude, respectively, and B and L are the

177 latitude and longitude in the initial region range. μ is the average value of the latitude or longitude, and
178 σ is the standard deviation of the latitude or longitude.

5

179   Third, determine the layered optimal polynomial function of the improved tomography model through
180   adaptive training.

- First, based on the size of the selected tomographic region, determine the highest
181
182   polynomial fit order. In this paper, the highest polynomial fit order chosen as 5 turns out to
183   be generally sufficient.
184   - Through obtaining the water vapor density from voxels penetrated by GNSS signal rays in
185   the tomographic region of each layer as the input value and constantly trying out new
186   polynomial functions, the optimal polynomial function of each layer is obtained by
187   simulated training.
188   During the processes of training and comparison, the number of voxels penetrated by GNSS
189   rays initially should be paid attention to since the number of estimated coefficients need to
190   be less than that of the voxels penetrated by GNSS rays in each layer. Under this premise,
191   the over-fitting problem should also be avoided, otherwise it would be counterproductive.
192   - Finally, after the comparison of training results of multi-group polynomial functions at
193   different levels, the polynomial function with the minimum RMSE value obtained from the
194   water vapor density of the post-fitting layer and that of the ECMWF results is the best fitting
195   equation for this layer. Each layer could have the individual optimal polynomial function in
196   general.

197   Fourth, after finding the optimal polynomial function of each layer in different heights, using the
198   latitude, longitude and altitude information into the function could obtain the three-dimensional water vapor
199   distribution of any position in the tomographic region. The three-dimensional water vapor field in the
200   tomographic zone can be described by broadcasting the estimated coefficients of the layered optimal
201   polynomial functions.

202   *2.3. The optimal polynomial selection based on adaptive training*

203   Since the polynomial form can better reflect the continuity of water vapor and has the advantage of
204   high-efficiency computing as well as easy expression, this paper chooses the polynomial form as the layered
205   fitting function. The selection process of the layered optimal polynomial function based on adaptive training
206   is as follows:

207   First, construct a polynomial equations training library, which contains a wide variety of polynomial
208   function forms of the latitude and longitude as independent variables while the water vapor density in the
209   voxels as the dependent variable. After many experiments, the maximum power of the latitude and
210   longitude found as 5 is sufficient to describe the water vapor changes. Therefore, the maximum power of
211   the fitting function part is adopted as 5 in the training library.

212   Second, according to the water vapor density observations from the voxels penetrated by the GNSS
213   signals at each level, the form of the candidate polynomial function of each layer is automatically
214   determined from the polynomial function training library to ensure that the number of observations at all
215   levels is always greater than the number of estimated coefficients of the candidate polynomials.

216   Third, calculate the water vapor variation index (WVVI) of each layer in both east-west and north-
217   south directions using the traditional tropospheric tomography results as shown in Eq. (10).

218
$$WVVI = \frac{\overline{\nabla wv_{EW}}}{\overline{\nabla wv_{NS}}} \tag{10}$$

219   where wv_{EW} and wv_{NS} are the water vapor density in east-west and north-south direction, separately.

220   The WVVI, a changing rate indicator of the water vapor density in a given direction, is obtained by
221   calculating the overall average change rate of the water vapor density in a given direction within each
222   adjacent voxel. According to the water vapor variation index of each layer in the east-west and north-south
223   direction, it can be determined whether the water vapor exists mainly in the east-west distribution or the
224   north-south distribution. As an aid, WVVI can choose the main body of the alternative polynomial function
225   with higher order term of the longitude or latitude for the subsequent accuracy comparison in order to
226   efficiently and quickly find the layered optimal polynomial function. If the water vapor density of a layer
227   indicates a horizontal gradient of east-west distribution, the polynomial function with higher-order term of
228   the longitude should be given the priority. It suggests that when the water vapor shows an east-west gradient
229   distribution there is a better correlation between the longitude and the water vapor variation, furthermore
230   the high-order term in longitude can better reflect the nuanced water vapor variation. A simple example of
231   the polynomial function with a higher-order term in longitude is shown in Eq. (11):

232     $$V_d = a_0 + a_1 B + a_2 L + a_3 BL + a_4 L^2 + a_5 BL^2 + a_6 L^3 \qquad (11)$$

233   Otherwise, when the water vapor density of a layer indicates a horizontal gradient of north-south
234   distribution, the polynomial function with higher-order term of the latitude should be given the priority. A
235   simple example is shown in Eq. (12):

236     $$V_d = a_0 + a_1 B + a_2 L + a_3 BL + a_4 B^2 + a_5 B^2 L + a_6 B^3 \qquad (12)$$

237   While the distribution regularities of the water vapor density gradient are not clear or obvious, the
238   polynomial function with the same order of the latitude and longitude can be considered as the example
239   shown in Eq. (13):

240     $$V_d = a_0 + a_1 B + a_2 L + a_3 BL + a_4 B^2 + a_5 L^2 \qquad (13)$$

241   Fourth, the candidate polynomials of all levels screened by the WVVI gradient auxiliary information
242   are used as the next comparative polynomials, and the required estimated coefficients of the comparative
243   polynomial are solved according to the principle of least squares through Eq. (14) and automatically
244   recorded into the coefficients data set. M is the matrix of the longitude and latitude, and the vector x
245   comprises the unknown coefficients of the comparative polynomial functions as shown in Eq. (15).

246     $$V_d = Mx \qquad (14)$$

247     $$x = \begin{bmatrix} a_0 \\ a_1 \\ \vdots \\ a_n \end{bmatrix} \qquad (15)$$

248   Fifth, through the comparative polynomials with the estimated coefficients in each layer, the whole-
249   voxel water vapor fitting of each layer is automatically fit with the information of the latitude and longitude.
250   In order to obtain the RMSE, the fitting result would be compared with the ECMWF water vapor density
251   of each layer in this period. The results are then saved to the accuracy data sets of each layer. The
252   comparative polynomials with the estimated coefficients are constantly selected to train the fitting of the

253   layered water vapor density and then compared with the water vapor density of ECMWF at each layer.

254   Thus, large accuracy data sets of RMSE can be obtained, where the smallest RMSE value of the

255   comparative polynomial form can be chosen, and then the optimal polynomial of each layer could come

256   into being. It is noteworthy that the optimal polynomial of each layer might be different. With the layered

257   optimal polynomial, the three-dimensional water vapor density in the tomographic region can be expressed

258   conveniently and continuously by transmitting the estimated coefficients information.

259 **3. Experiment**

260 *3.1. Experimental description and data-processing strategy*

261   To study whether the accuracy and stability of the results of the improved tropospheric tomography

262   model are better than the traditional pixel-based tropospheric tomography model, the following experiment

263   is designed.

264   Tomographic data is obtained from the SatRef Network for Hong Kong from 25 March 2014 to 25

265   April 2014. Two epochs are taken each day (0:00 and 12:00 UTC). The corresponding meteorological data

266   is also used to calculate the PWV. The tomographic area ranges between latitude 22.24°N to 22.54°N and

267   longitude 113.87°E to 114.29°E. Taking the mean sea level as the height of the base level, the vertical

268   resolution is 0.8 km, and total grid number is $5 \times 7 \times 13$. In the selected area, a total of 11 GNSS stations

269   and 1 radiosonde station (located at King's Park, Hong Kong) are selected, and the ECMWF grid data are

270   extracted twice daily at 00:00 and 12:00 UTC from 25 March 2014 to 25 April 2014 (grid resolution of

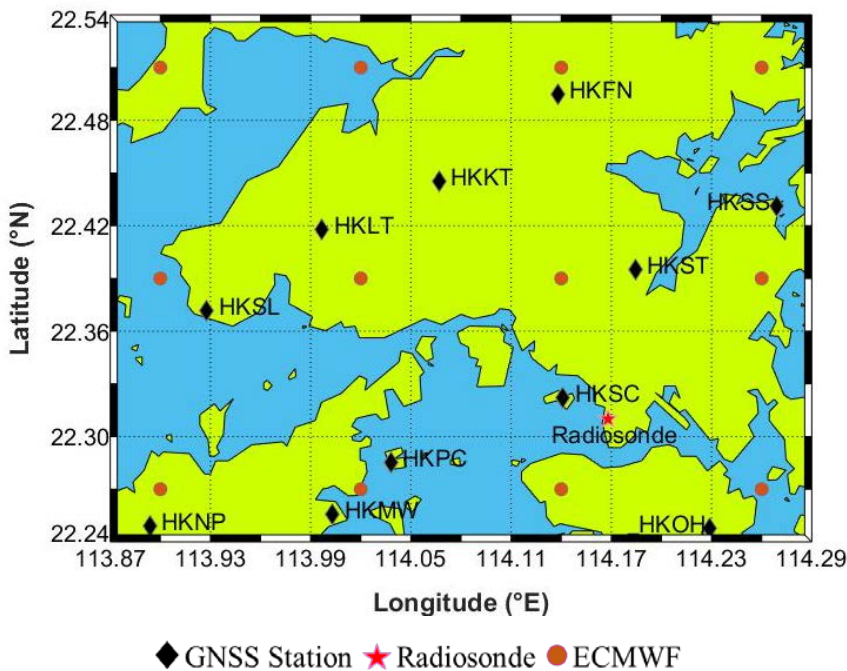271 0.125×0.125). See Fig. 1 for details.

272

Figure 1. The GNSS stations (11 black rhombuses) and the radiosonde station (1 red star) and the ECMWF comparative

275 points (12 ochre circles) in Hong Kong. The grid lines display tomography grids.

276   According to the official website of the Hong Kong Observatory

277 (http://www.weather.gov.hk/contentc.htm) for the weather review, Hong Kong had a total of 15 days of

278 rainy weather from 25 March 2014 to 25 April 2014, as shown in Table 1.

279

Table 1. Rainfall information for March and April 2014.

Date	Rainfall situation
3.29	Thunderstorms turn to heavy rain
3.30	Thunderstorms turn to heavy rain
3.31	Thunderstorms turn to heavy rain
4.1	Showers accompanied by wind, thunderstorms
4.2	Showers, reports of hail in some areas
4.3	Showers, some parts of the rain are quite large
4.6	Cloudy showers, low temperature
4.7	Heavy showers, low temperature
4.8	Showers, low temperature
4.14	Showers
4.21	Cloudy turns to the showers
4.22	Showers and foggy
4.23	Showers turn to the rain
4.24	Showers turn to the cloudy
4.25	Cloudy turns to the rain

280   In this paper, GAMIT (v10.50) (Herring et al., 2010) software was used for processing the GPS
281 observations based on the double-differenced model at a sampling interval of 30 s, and the global mapping
282 function was adopted. The zenith total delay (ZTD) and wet horizontal gradient intervals were estimated at
283 0.5 h and 2 h, respectively. Based on the surface pressure obtained from observed meteorological
284 parameters, the ZHD could be obtained by the Saastamoinen model, and ZWD was isolated from ZHD.
285 Via GMF projection, the SWD could be obtained by transforming the observed SWV.

3.2. Experimental introduction and program comparison

287   The RMSE and bias of the improved tomography model residuals were calculated by subtracting the
288 ECMWF water vapor density from the water vapor density of the improved pixel-based water vapor
289 tomography model (hereinafter referred to as improved tomography model). In a similar way, the RMSE
290 and bias of the traditional tomography model residuals can also be obtained from the difference between
291 the ECMWF water vapor density and the three-dimensional water vapor density obtained by the traditional
292 pixel-based tropospheric tomography model (hereinafter referred to as the traditional tomography model).

293   In the period of data processing, the situation can be compared on a case-by-case basis to
294 comprehensively evaluate the accuracy of the improved tomography model from various views. In this
295 paper, 6 scenarios are investigated, comprising the spatial distribution scenario, the everyday distribution
296 scenario, the rainy scenario and the non-rainy scenario. Moreover the residuals of the water vapor density
297 in voxels with and without penetrating GNSS rays are inspected. The definitions of 6 scenarios
298 abovementioned are as follows:

299   The spatial distribution scenario is investigated by obtaining the RMSE and bias of the residuals from
300 all ECMWF comparative points at all time intervals as well as the layered tomography accuracy.

301   The everyday distribution scenario is found by obtaining the RMSE and bias of the residuals from all
302 ECMWF comparative points in two epochs each day, and the overall accuracy of 32 days between 25 March
303 2014 and 25 April 2014 was calculated.

304   The rainy scenario is based on the distribution of 15 days of rainy days between 25 March and 25
305 April, 2014, as referred to in Table 1, in which the RMSE and bias of the residuals are obtained from all

306 ECMWF comparative points in all the epochs in rainy days for the further accuracy analysis. Similarly, the
307 non-rainy scenario is found with the accuracy analysis of the non-rainy days.

308   The scenario of residuals of the water vapor density in voxels without GNSS rays penetration is found
309 by obtaining the RMSE and bias of the residuals from ECMWF comparative points without rays passing
310 through in all the epochs each day. Conversely, the scenario with GNSS rays penetration is found by
311 obtaining the RMSE and bias of the residuals from ECMWF comparative points with rays passing through
312 in all the epochs each day.

313   According to the above classifications, the accuracy of the improved tomography model residuals and
314 the traditional tomography model residuals were calculated, and the accuracy of the new model was
315 compared with the traditional model to determine which one is better. Furthermore, the accuracy
316 comparison of the water vapor density derived from two models and radiosonde data was designed to show
317 if the improved model would be more efficient than the traditional one.

318 **4. Interpretation of 6 scenario results**

319 *4.1. Accuracy information of the spatial distribution scenario*

320   To verify whether the accuracy of the improved tomography model is better than that of the traditional
321 tomography model, the layered RMSE and bias of the residuals from all ECMWF comparative points at all
322 time intervals between the tomography (using both the optimal polynomial function of each layer and the
323 traditional way) and the ECMWF results are obtained and shown in Table 2, and the calculation of RMSE
324 improvement percentage involved in the following tables is shown in Eq. (16).

$$325 \quad \Delta RMSE\% \ = \left(RMSE_{trad} - RMSE_{impr} \right) / RMSE_{trad} \cdot 100\% \quad (16)$$

326 where $RMSE_{impr}$ is the RMSE value of the residuals calculated from the improved tomography model,

327 and $RMSE_{trad}$ is the RMSE value of the residuals obtained from the traditional tomography model.

328   Table 2 shows that RMSE and bias values obtained by the improved tomography model are smaller
329 than those of the traditional tomography model, and the RMSE improvement percentage is positive, which
330 indicates that the improved tomography model has a higher accuracy than the traditional tomography model
331 overall. Moreover, the RMSE improvement percentage is appreciable in the upper region because the value
332 of the water vapor density in high altitude is very small (see Fig. 2 for details), even the small changes in
333 the upper region could result in a large percentage change. In addition, the bias and RMSE in the bottom
334 from Table 2 are not as good as those of the other higher layers, regardless of which model is used. These
335 results could be mainly ascribed to a certain system deviation between the comparison data of ECMWF
336 and the GNSS tomographic data. Besides, the observations and the number of redundant observations are
337 insufficient due to less voxels with GNSS rays penetration in the bottom, resulting in the low accuracy.
338 What's more, Figure 2 shows that the water vapor content in the bottom region is too abundant and
339 changeable to be generally described accurately. These above reasons lead to large bias and RMSE values
340 in the bottom tropospheric area.

341 **Table 2.** Statistics of two models' tomography accuracy with respect to ECMWF data in the spatial distribution scenario
342 for the experimental period (Unit: g/m^3).

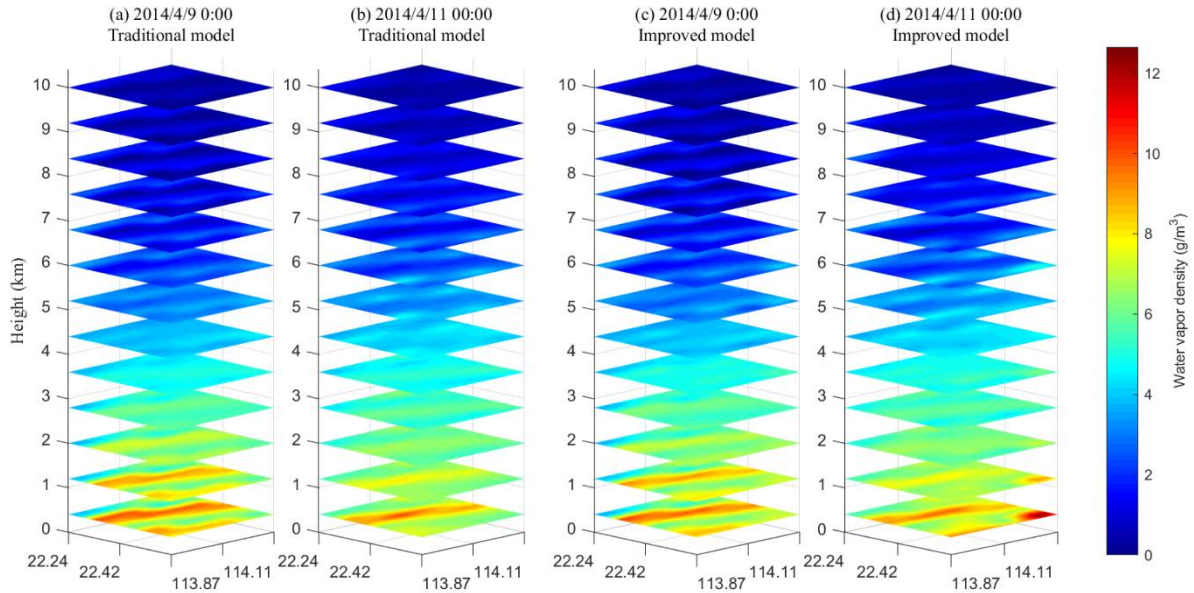| Layer	bias		RMSE		RMSE Improvement Percentage
	Traditional model	Improved model	Traditional model	Improved model	
1	-7.81	-7.65	8.17	8.00	2.06%
2	-3.52	-3.42	3.95	3.83	3.14%
3	-0.90	-0.80	1.66	1.60	4.05%
4	0.72	0.61	1.39	1.36	2.00%
5	1.62	1.58	1.87	1.83	2.28%
6	1.95	1.77	2.10	2.09	0.39%
7	1.98	1.90	2.25	2.20	2.07%
8	1.76	1.68	2.15	2.10	2.32%
9	1.62	1.60	2.06	2.04	1.10%
10	1.34	1.11	1.85	1.47	20.68%
11	1.04	0.87	1.60	1.25	21.75%
12	0.74	0.61	1.26	0.96	23.67%
13	0.44	0.38	0.71	0.58	18.36%

343 **Figure 2.** The layered maps of the water vapor density from **(a) (b)** the traditional model and **(c) (d)** the improved
344 model at specific epochs, **(a) (c)** 0:00 UTC 9 April 2014 and **(b) (d)** 0:00 UTC 11 April 2014.

345 *4.2. The accuracy information of the everyday distribution scenario*

346   To determine whether the accuracy of the improved tomography model is better than that of the
347 traditional tomography model on the everyday time scale, the RMSE improvement percentage is obtained
348 from all ECMWF comparative points (a total of 12) at two epochs each day using both the layered optimal
349 polynomial functions and the traditional method. Figure 3 shows that the percentage of RMSE improvement
350 per day is practically positive, and the percentage of April 11th can even approach 12%, indicating that the
351 improvement seems to be appreciable. This improvement shows that the accuracy of the improved
352 tomography model is mostly superior to that of the traditional tomography model in everyday distribution;

11

however, on April 7, April 9 and April 15, the RMSE improvement percentage is negative. This might be due to the heavy showers bringing rapid water vapor changes from April 7 to April 8 and on April 14, which is difficult to fit the polynomial function well with the unstable water vapor. However, since negative percentages do not exceed -1%, the accuracy of these four days calculated by the improved tomography model could be considered basically equivalent to that of the traditional tomography model.
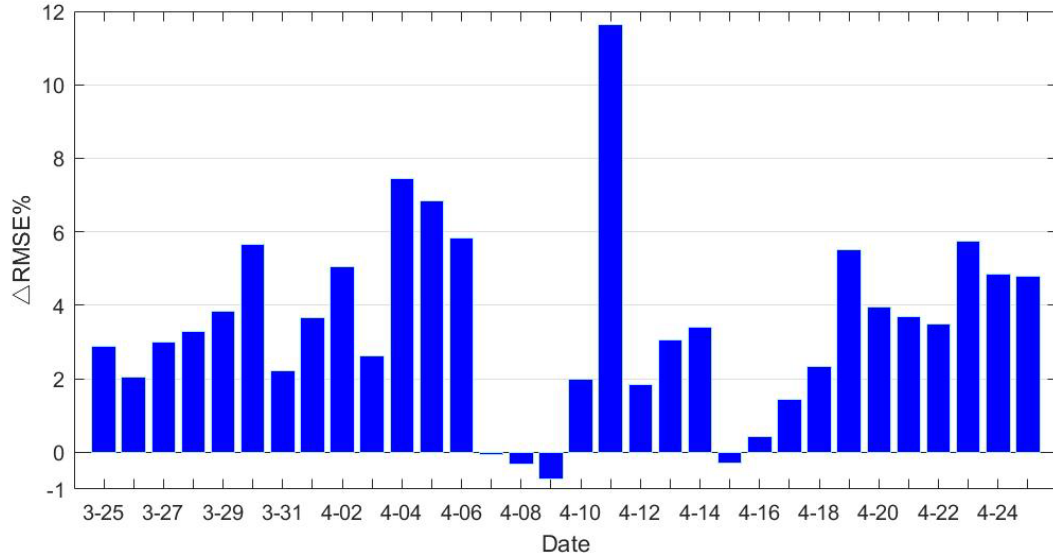

Figure 3. Everyday distribution statistics of daily RMSE improvement percentage between 25 March and 25 April, 2014.

In addition, the overall RMSE and bias of the residuals are obtained from the ECMWF comparative points (a total of 12) in two epochs under the entire everyday distribution scenario. The statistical results are shown in Table 3 below.

Table 3. Statistics of two models' tomography accuracy with respect to ECMWF data in the everyday distribution scenario for the experimental period (Unit: g/m^3).

Statistics type	Traditional model	Improved model	RMSE improvement percentage
RMSE	2.97	2.87	3.44%
bias	0.07	0.02	

Table 3 shows that the RMSE obtained by the improved model is smaller by 3.44% compared to the traditional one. The bias of the improved model more closes to zero, indicating that the improved tomography model has better stability and less systematic deviation from the comparative data. The better accuracy of the improved model compared to the traditional one illustrates the edge of the improved model.

4.3. The accuracy information of rainy and non-rainy scenarios

To further analyze the reliability of the improved tomography model compared with the traditional tomography model in different weather conditions, according to the distribution of rainy days in Table 1, all the rainy days data and non-rainy days data are used separately for tomography to obtain the RMSE and bias of the residuals under corresponding weather conditions. The number of matching points is still 12 (see Fig. 1). The overall statistical results are shown in Table 4.

Table 4. Statistics of two models' tomography accuracy with respect to ECMWF data in the rainy scenario and the non-rainy scenario for the experimental period (Unit: g/m^3).

(a) The overall rainy scenario statistics			
Statistics type	Traditional model	Improved model	RMSE improvement percentage
RMSE	3.05	2.94	3.68%
bias	0.05	-0.01	
(b) The overall non-rainy scenario statistics			
Statistics type	Traditional model	Improved model	RMSE improvement percentage
RMSE	2.89	2.80	3.21%
bias	0.10	0.04	

Table 4 (a) shows that the RMSE and bias of the residuals calculated by the improved tomography model are better than those of the traditional tomography model using rainy days' data. The RMSE of the improved tomography model is 3.68% higher than that of the traditional model, indicating the accuracy of the new model is superior. The improved model bias closes more to zero than that of the traditional one, which means the new model has an increase in stability and a reduction in the system error. Using non-rainy days' data, the RMSE and bias of the residuals calculated by the improved tomography model are also better than those of the traditional tomography model, see Table 4 (b). The RMSE improvement percentage is 3.21%, also indicating there is an improvement in the accuracy of the new model. Besides, the improved model bias is more close to zero, making the system error weakened and the stability enhanced. According to the RMSE improvement percentage under the rainy and non-rainy scenarios, the RMSE improvement percentage of rainy days is better than that of non-rainy days. This finding shows that the improved tomography model is more suitable for obtaining the tomographic results when severe water vapor changes occur.

4.4. The accuracy information of voxels with and without GNSS rays penetrating scenarios

In the traditional pixel-based water vapor tomography model, the water vapor density in the voxels without GNSS rays passing through depends on the accuracy of the water vapor density in the adjacent voxels with GNSS rays penetration. However, the improved tomography model uses the layered optimal polynomial function for overall fitting to obtain the water vapor density in voxels without penetrating GNSS rays. To determine whether the layered optimal polynomial function of the improved method contributes better to the accuracy of the water vapor density, the scenarios of voxels with and without GNSS rays penetration as described in section 3.2 were designed. After obtaining the RMSE and bias of the residuals using the improved and traditional tomography models separately under designed scenarios, the overall accuracy information of voxels with and without GNSS rays penetrating shows in Table 5.
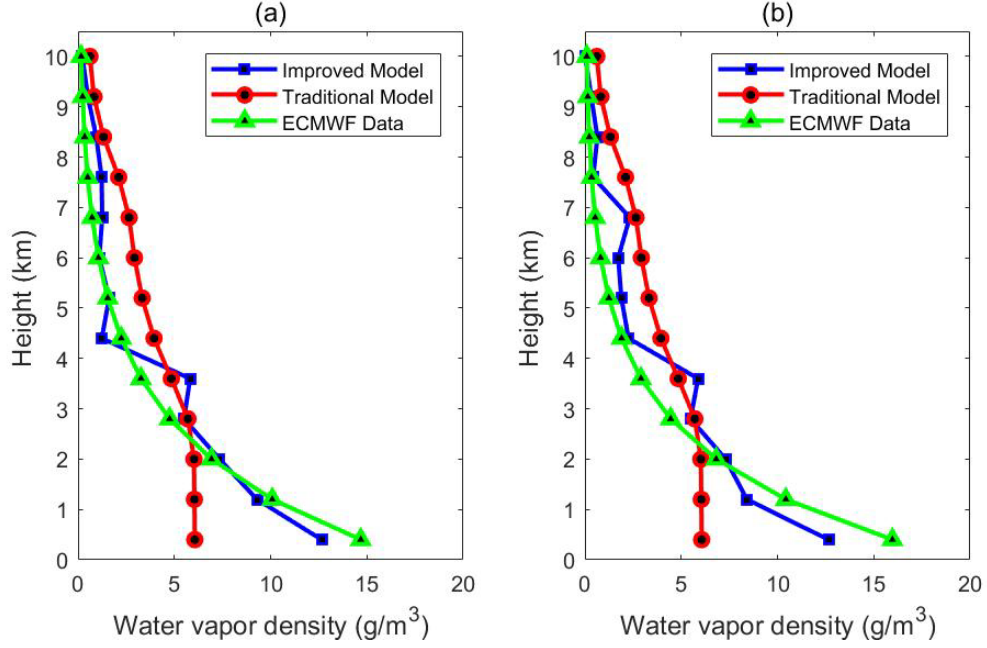
Table 5. Statistics of two models' tomography accuracy with respect to ECMWF data in the voxels with and without penetrating GNSS rays for the experimental period (Unit: g/m^3).

(a) The overall scenario statistics of voxels without rays penetrating			
Statistics type	Traditional model	Improved model	RMSE Improvement Percentage
RMSE	3.40	3.20	5.88%
Bias	1.59	1.51	
(b) The overall scenario statistics of voxels with rays penetrating			
Statistics type	Traditional model	Improved model	RMSE Improvement Percentage
RMSE	3.27	3.24	1.00%
bias	1.70	1.65	

Table 5 (a) shows that the RMSE and bias of the residuals calculated by the improved tomography model are better than those of the traditional tomography model in the scenario of voxels without GNSS rays penetrating. Moreover the RMSE of improved tomography model is 5.88% better than that of the traditional tomography model, and the bias decreased from 1.59 to 1.51 g m^{-3}. To a certain extent, this finding shows that the improved tomography model is more advantageous for obtaining the water vapor density from the voxels without GNSS rays penetrating, which is consistent with the initial hypothesis: the traditional tomography model uses empirical constraint equations in section 2.1.2, Eq. (7), which is unable to well represent the distribution of the water vapor density from voxels without GNSS rays penetrating in the actual situation. However, the new proposed model uses the relatively exact water vapor density from voxels with GNSS rays penetrating as the observation values to further fit the water vapor density in voxels without GNSS rays penetrating. Therefore, the improved tomography model can better reflect the actual layered situation of continuous water vapor changes, and the accuracy is naturally better. What's more, the RMSE and bias obtained by the improved tomography model are also superior to those of the traditional tomography models using the classified data of voxels with GNSS rays penetrating, see Table 5 (b). The RMSE calculated by the new model is 1% higher than that of the traditional model, and the bias reduced from 1.7 to 1.65 g m^{-3}. In summary, whether it is calculated separately from data of voxels with or without GNSS rays penetrating, the results of the improved tomography model are superior to those of the traditional tomography model to a certain extent, which could prove the advanced nature and reliability of the improved tomography model.

In order to double-check if the improved tomography model in the scenario of voxels without GNSS rays passing through shows a better result in the vertical distribution of the three-dimensional water vapor density, the water vapor density profiles for different altitudes at individual times are given in Fig. 4. Two times (0:00 UTC 11 April 2014 and 12:00 UTC 11 April 2014) are chosen for they correspond to the maximum percentage of RMSE improvement during the experiment period of 32 days. Figure 4 shows that in the scenario of voxels without GNSS rays penetration, the water vapor profile of the improved tomography model better matches that of ECMWF data than the traditional tomography model at both times, especially in the bottom layers, which again implies that the water vapor density derived from the improved model is superior to that of the traditional one in the scenario of voxels without penetrating GNSS

14

431   rays.

432

433   **Figure 4.** Water vapor profiles derived from ECMWF and two models in the scenario of voxels without penetrating

434   GNSS rays, **(a)** and **(b)** are periods of 0:00 UTC 11 April 2014 and 12:00 UTC 11 April 2014, respectively.

435   Furthermore, to compare directly the vertical accuracy of the water vapor density derived from

436   different altitudes in the scenario of voxels without penetrating GNSS rays, the tomographic results (25

437   March 2014 to 25 April 2014) from two different tomography models are analyzed. Figure 5 shows the

438   percentage of RMSE improvement and the relative error of the water vapor density changing with altitudes.

439   The percentage of RMSE improvement in Fig. 5 is defined as the same as Eq. (16), and the relative error is

440   defined by using the Eq. (17).

441    $$RE = \frac{\rho - \rho_{ECMWF}}{\rho_{ECMWF}} \qquad (17)$$

442   where *RE* is the relative error, ρ represents the water vapor density derived from the traditional or

443   improved tomography model, and ρ_{ECMWF} is the water vapor density derived from ECMWF grid data.

444   It can be observed in Fig. 5 that in the scenario of voxels without GNSS rays penetration the percentage

445   of RMSE improvement is positive in lower layers while negative in some middle and upper layers, which

446   could prove that the proposed model improves the accuracy of tomography results in most layers when

447   there are seldom voxels with GNSS rays penetrating especially in the bottom layers. Due to the lack of

448   GNSS observation data, the bottom accuracy of tomographic results is generally low. In addition, Figure 5

449   shows in the scenario of voxels without GNSS rays penetration, the relative error begins to decrease with

450   the altitude and then increases above 3 km. When the altitude is higher, the relative error becomes larger

451   because of the small water vapor values of the upper layers, a very tiny difference could cause a large

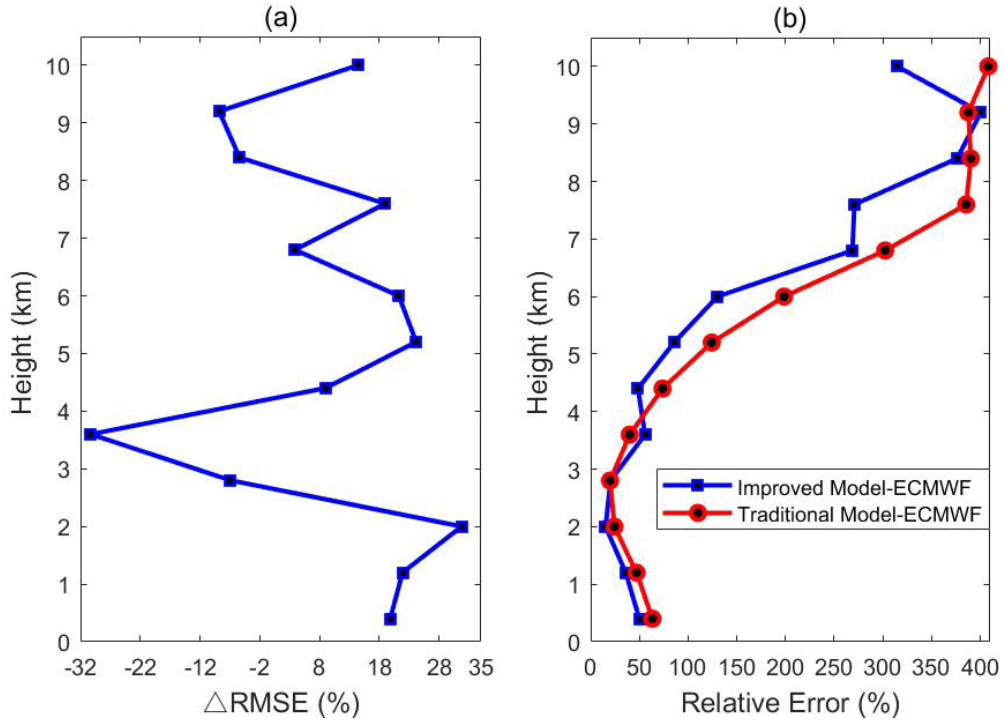452   relative error between the models and the ECMWF data.

15

Figure 5. In the scenario of voxels without GNSS rays penetration **(a)** the percentage of RMSE improvement and **(b)** the relative error change with height (the blue curve and red curve are derived from the differences between the profiles of the improved tomography model, the traditional tomography model and ECMWF grid data, separately for 64 epochs from 25 March 2014 to 25 April 2014).

5. Water vapor comparison with radiosonde data

As radiosonde data can provide fairly accurate vertical profiles of tropospheric water vapor (Niell et al., 2001), in this paper, the water vapor profiles derived from radiosonde data, as a reference, are used to validate the tomographic results from two models for showing if the improved model would be more efficient than the traditional one. In Hong Kong, there is one radiosonde station located at King's Park (shown in Fig. 1) where radiosonde balloons are launched twice daily at 0:00 and 12:00 UTC, respectively. The water vapor profiles derived from the improved model and the traditional model for the location of the radiosonde station are compared with that from radiosonde data at 00:00 and 12:00 UTC daily for the experimental period of 32 days. The overall statistical results are shown in Table 6. The RMSE and the bias of the improved model are 2.24 and -0.34 g m^{-3}, respectively, and the values using the traditional model are 2.13 and -0.46 g m^{-3}, respectively, which indicates that the RMSE of the improved model is not as good as the traditional model while the bias of the improved model is a little better than that of the traditional one. The reason for poor accuracy of the improved model could be due to systematic differences between the training source ECMWF data and the radiosonde data as the water vapor density of the improved model is obtained by the optimal polynomial selection based on adaptive training with ECMWF data. Besides, shown in Fig.1, the location of the radiosonde station is close to one GNSS station (HKSC), leading to the voxels for the location of the radiosonde station having GNSS rays penetration. Since the improved model has advantages of obtaining water vapor density just from voxels without GNSS rays penetration, this situation cannot show the superiority of the improved model.

16

476   **Table 6.** Statistics of two models' tomography accuracy with respect to radiosonde data for the experimental period
477   (Unit: g/m^3).

Statistics type	Traditional model	Improved model
RMSE	2.13	2.24
bias	-0.46	-0.34

478   In addition, water vapor profiles obtained by two models and radiosonde data are compared for the
479   specific two epochs at 0:00 UTC 25 March 2014 and 0:00 UTC 7 April 2014, shown in Fig. 6. Those two
480   times are selected because they correspond to the non-rainy day and heavy rainfall day, which could be
481   more comprehensive and representative for the comparison results of water vapor profiles. It can be seen
482   from Fig. 6 that no matter in the non-rainy day or the rainy day, both the improved model and the traditional
483   model can hardly match the radiosonde data at most altitudes, especially at the lower layers, showing again
484   this radiosonde data comparison experiment design cannot reflect the superiority of the improved model.
485   However, Figure 6 also shows the water vapor profiles of the improved model almost match that of the
486   traditional model, whether it is non-rainy or rainy, indicating that though both under the situation of poor
487   water vapor profile matching results the improved model still has the advantage of the convenient and
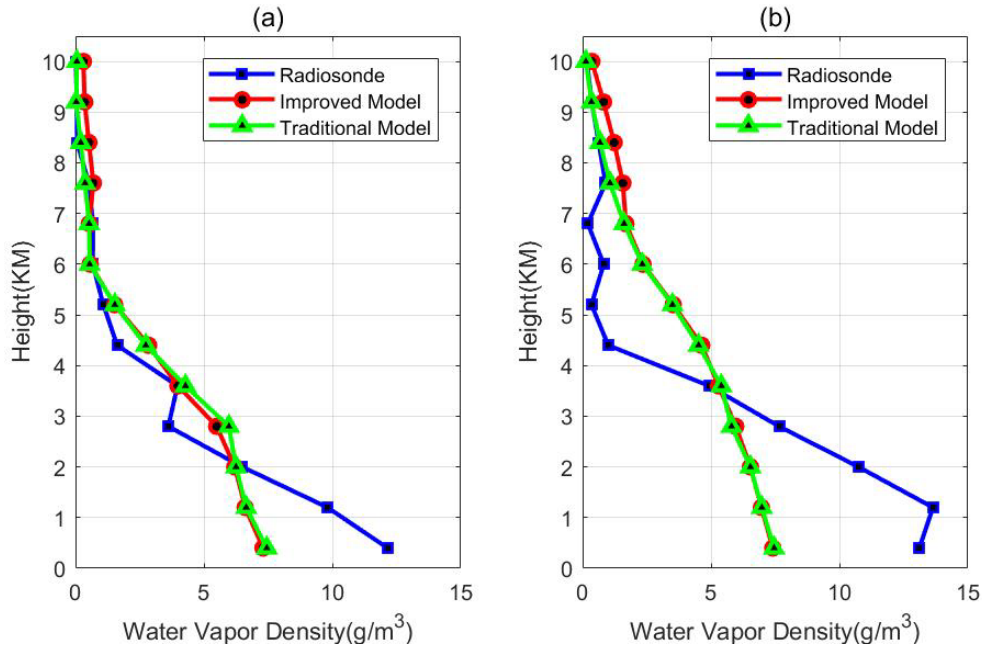488   efficient expression.

489   **Figure 6.** Water vapor profile comparison derived from different tomographic methods and radiosonde, **(a)** a non-rainy
490   day at 0:00 UTC 25 March 2014, **(b)** a rainy day at 0:00 UTC 7 April 2014.

491   **6. Conclusion**

492   In this paper, an improved pixel-based water vapor tomography model has been proposed, which is
493   much more concise and convenient in expression than the traditional one. Only the optimal polynomial
494   coefficients of each layer are required to describe the three-dimensional water vapor distribution in the
495   tomographic region. By using the SatRef GNSS network observation data in Hong Kong between 25 March
496   and 25 April, 2014, the RMSE and bias have been assessed in 6 scenarios. The scenarios include the spatial
497   distribution scenario and the everyday distribution scenario, the rainy scenario and the non-rainy scenario,
498   and the voxels with and without GNSS rays penetrating scenarios. The results demonstrate that in either

499 case, the RMSE and bias of the improved tomography model are better than that of the traditional
500 tomography model. Among these scenarios, when there are voxels without GNSS rays penetrating, the
501 RMSE improvement percentage can be significantly increased up to 5.88%, which shows that the improved
502 tomography model is more advantageous for obtaining the water vapor density from voxels without GNSS
503 rays penetration. Using radiosonde data for evaluation, it is proved that with the almost similar accuracy
504 the improved model is more efficient in expression than the traditional one. However, some shortcomings
505 remain in the improved GNSS tropospheric tomography model. For example, when constructing the
506 optimal polynomial of each layer, the polynomial is not only limited by the water vapor density quality in
507 voxels with GNSS rays passing through calculated by the traditional pixel-based tomography model, but it
508 is also limited by the size of the tomographic area and the situation of dividing voxels. In the future, the
509 function-based water vapor tomography model should be further studied, which is free from the above
510 limitations. It is expected that the function-based tropospheric tomography model will be more conveniently
511 used when the expression parameters of the function part could be obtained directly from SWVs.

516 **References**

517 Adavi, Z. and Mashhadi-Hossainali, M.: 4D-tomographic reconstruction of water vapor using the hybrid
518 regularization technique with application to the North West of Iran, Adv. Space Res., 55, 1845-1854, 2015.
519 Aghajany, S. H. and Amerian, Y.: Three dimensional ray tracing technique for tropospheric water vapor
520 tomography using GPS measurements, J. Atmos. Sol.-Terr. Phys., 164:81-88, 2017.
521 Alber, C., Ware, R., Rocken, C., and Braun, J. J.: Obtaining single path phase delays from GPS double
522 differences, Geophys. Res. Lett., 27, 2661–2664, 2000.
523 Baltink, H. K., Marel, H. V. D., and Der Hoeven, A. V.: Integrated atmospheric water vapor estimates from
524 a regional GPS network, J. Geophys Res-Atmos., 107, ACL 3-1–ACL 3-8, 2002.
525 Bender, M., Stosius, R., Zus, F., Dick, G., Wickert, J., and Raabe, A.: GNSS water vapour tomography –
526 Expected improvements by combining GPS, GLONASS and Galileo observations, Adv. Space Res., 47,
527 886-897, 2011.
528 Bevis, M., Businger, S., Chiswell, S. R., Herring, T. A., Anthes, R. A., Rocken, C., and Ware, R.: GPS
529 meteorology: mapping zenith wet delays onto precipitable water, J. Appl. Meteorol., 33, 379-386, 1994.
530 Bi, Y., Mao, J., and Li, C.: Preliminary results of 4-D water vapour tomography in the troposphere using
531 GPS, Adv. Atmos. Sci., 23, 551–560, 2006.
532 Bock, O., Keil, C., Richard, E., Flamant, C., and Bouin, M.: Validation of precipitable water from ECMWF
533 model analyses with GPS and radiosonde data during the MAP SOP, Q. J. Roy. Meteorol. Soc., 131, 3013-
534 3036, 2005.
535 Braun, J. J., Rocken, C., Meertens, C., and Ware, R.: Development of a Water Vapor Tomography System
536 Using Low Cost L1 GPS Receivers, in: Ninth ARM Science Team Meeting Proceedings, San Antonio,
537 Texas, 22-26 March 1999, 1-6, 1999.
538 Braun, J. J., Rocken, C., and Liljegren, J. C.: Comparisons of line-of-sight water vapor observations using
539 the global positioning system and a pointing microwave radiometer, J. Atmos. Ocean. Tech., 20, 606-612,
540 2003.

541   Braun, J. J.: Remote sensing of atmospheric water vapor with the global positioning system, Ph.D. thesis,

542   University of Colorado, 2004.

543   Cao, Y.: GPS Tomographying Three-Dimensional Atmospheric Water Vapor and Its Meteorological

544   Applications, Ph.D. Thesis, The Chinese Academy of Sciences, Beijing, China, 2012.

545   Chen B. and Liu Z.: Voxel-optimized regional water vapor tomography and comparison with radiosonde

546   and numerical weather model, J. Geodesy, 88, 691-703, 2014.

547   Ding, N., Zhang, S. B., Wu, S.Q., Wang, X. M., and Zhang, K. F.: Adaptive node parameterization for

548   dynamic determination of boundaries and nodes of GNSS tomographic models, J. Geophys. Res-Atmos.,

549   123, 1990-2003, 2018.

550   Dong Z. and Jin S.: 3-D Water Vapor Tomography in Wuhan from GPS, BDS and GLONASS Observations,

551   Remote Sens., 10(1):62, 2018.

552   Emardson, T. R., Elgered, G., and Johansson, J. M.: Three months of continuous monitoring of atmospheric

553   water vapor with a network of Global Positioning System receivers, J. Geophys. Res., 103, 1807-1820,

554   1998.

555   Flores, A., Ruffini, G., and Rius, A.: 4D tropospheric tomography using GPS slant wet delays, Ann.

556   Geophys. Ger., 18, 223-234, 2000.

557   Guo, J., Yang, F., Shi, J., and Xu, C.: An Optimal Weighting Method of Global Positioning System (GPS)

558   Troposphere Tomography, IEEE J-STARS., 9(12), 5880-5887, 2016.

559   Herring, T. A., King, R. W., and McClusky, S. C.: Documentation of the GAMIT GPS Analysis Software

560   release 10.4. Department of Earth and Planetary Sciences, Massachusetts Institute of Technology,

561   Cambridge, Massachusetts, 2010.

562   Hirahara K.: Local GPS tropospheric tomography, Earth Planets Space, 52, 935-939, 2000.

563   Liu, Y., Chen, Y., and Liu, J.: Determination of weighed mean tropospheric temperature using ground

564   meteorological measurements, Geospatial Inf. Sci., 4, 14-18, 2001.

565   Macdonald, A. E., Xie, Y., and Ware, R. H.: Diagnosis of Three-Dimensional Water Vapor Using a GPS

566   Network, Mon. Weather Rev., 130, 386-397, 2002.

567   Marel, H. V. D.: Virtual GPS reference stations in the Netherlands, in: Proceedings of ION GPS-98,

568   Nashville, TN, 15-18 September, pp. 49-58, 1998.

569   Niell, A. E., Coster, A. J., Solheim, F. S., Mendes, V. B., Toor, P. C., Langley, R. B., and Upham, C. A.:

570   Comparison of measurements of atmospheric wet delay by radiosonde, water vapour radiometer, GPS, and

571   VLBI, J. Atmos. Ocean. Tech., 18, 830–850, 2001.

572   Nilsson, T. and Gradinarsky, L.: Water vapor tomography using GPS phase observations: simulation results,

573   IEEE T. Geosci. Remote, 44, 2927-2941, 2006.

574   Perler, D., Geiger, A., Hurter, F.: 4D GPS water vapor tomography: new parameterized approaches, J.

575   Geodesy, 85, 539-550, 2011.

576   Rocken, C., Van Hove, T., and Ware, R.: Near real‐time GPS sensing of atmospheric water vapor, Geophys.

577   Res. Lett., 24, 3221-3224, 1997.

578   Rohm, W. and Bosy, J.: Local tomography troposphere model over mountains area, Atmos. Res., 93, 777-

579   783, 2009.

580   Rohm, W., Zhang, K., and Bosy, J.: Limited constraint, robust Kalman filtering for GNSS troposphere

581   tomography, Atmos. Meas. Tech., 6, 1475-1486, 2014.

582   Saastamoinen, J.: Atmospheric Correction for the Troposphere and Stratosphere in Radio Ranging Satellites,

583   The use of Artificial Satellites for Geodesy, 15, 247-251, 1972.

584 Seko, H., Shimada, S., Nakamura, H., and Kato, T.: Three-dimensional distribution of water vapor
585 estimated from tropospheric delay of GPS data in a mesoscale precipitation system of the Baiu front, Earth
586 Planets Space, 52, 927-933, 2000.

587 Troller, M., Burki, B., Cocard, M., Geiger, A., and Kahle, H. G.: 3-D refractivity field from GPS double
588 difference tomography, Geophys. Res. Lett., 29, 2-1–2-4, 2002.

589 Vollach, U., Buecherl, A., Landau, H., Pagels, C., Wagner, B.: Multi-Base RTK Positioning Using Virtual
590 Reference Stations, in: Proceedings of ION GPS-2000, Salt Lake City, 19-22 September 2000, 123-131,
591 2000.

592 Weckwerth, T. M., Parsons, D. B., Koch, S. E., Moore, J. A., Lemone, M. A., Demoz, B., Flamant, C.,
593 Geerts, B., Wang, J., and Feltz, W. F.: An overview of the international H2O project (IHOP_2002) and some
594 preliminary highlights, B. Am. Meteorol Soc., 85, 253-277, 2004.

595 Yao, Y. B., Zhao, Q. Z., and Zhang, B.: A method to improve the utilization of GNSS observation for water
596 vapor tomography, Ann. Geophys., 34, 143-152, https://doi.org/10.5194/angeo-34-143-2016, 2016.

597 Yao, Y., Chen, P., Zhang, S., and Chen, J.: A new ionospheric tomography model combining pixel-based
598 and function-based models, Adv. Space Res., 52, 614-621, 2013.

599 Zhao, Q. and Yao, Y.: An improved troposphere tomographic approach considering the signals coming from
600 the side face of the tomographic area, Ann. Geophys., 35, 87-95, https://doi.org/10.5194/angeo-35-87-2017,
601 2017.

602 Zhao, Q., Yao, Y., Yao, W., and Xia, P.: An optimal tropospheric tomography approach with the support of
603 an auxiliary area, Ann. Geophys., 36, 1037-1046, https://doi.org/10.5194/angeo-36-1037-2018, 2018.